

A Phase Diagram Unifies Energy Dissipation, Kinetics, and Rheology in Inertial Granular Flows

E. DeGiuli¹, J.N. McElwaine², and M. Wyart³

¹*New York University, Center for Soft Matter Research,
4 Washington Place, New York, NY, 10003,*

²*Department of Earth Sciences, Durham University,
Science Labs, Durham, DH1 3LE, U.K.*

³*Institute of Theoretical Physics,
Ecole Polytechnique Fédérale de Lausanne (EPFL),
CH-1015 Lausanne, Switzerland*

Flows of hard granular materials depend strongly on the interparticle friction coefficient μ_p and on the inertial number \mathcal{I} , which characterizes proximity to the jamming transition where flow stops. Guided by numerical simulations, we derive the phase diagram of dense inertial flow of spherical particles, finding three regimes for $10^{-4} \lesssim \mathcal{I} \lesssim 0.1$: *frictionless*, *frictional sliding*, and *rolling*. These are distinguished by the dominant means of energy dissipation, changing from collisional to sliding friction, and back to collisional, as μ_p increases from zero at constant \mathcal{I} . The three regimes differ in their kinetics and rheology; in particular, the velocity fluctuations and the stress anisotropy both display non-monotonic behavior with μ_p , corresponding to transitions between the three regimes of flow. We characterize the scaling properties of these regimes, show that energy balance yields scaling relations for each of them, and explain why friction qualitatively affects flow.

Dense flows of granular media are central to many industrial processes and geophysical phenomena, including landslides and earthquakes [1–3]. At a fundamental level, describing such driven materials remains a challenge, in particular near the jamming transition where crowding effects become dominant and flow stops. In the last decade, progress was made by considering the limit of *perfectly rigid* grains, for which dimensional analysis implies that the strain rate $\dot{\epsilon}$, the pressure P and the grain density ρ can only affect flows via the inertial number $\mathcal{I} = \dot{\epsilon}D\sqrt{\rho/P}$, where D is grain diameter [4–6]. In particular, for stationary flows the packing fraction ϕ and stress anisotropy $\mu = \sigma/P$, where σ is the shear stress, are functions of \mathcal{I} . From the constitutive relations $\phi(\mathcal{I})$ and $\mu(\mathcal{I})$ the flow profile can be explained in simple geometries [4, 7, 8]. Here we focus on dense flows $\mathcal{I} \lesssim 0.1$ for which the networks of contacts between grains span the system and particle motion is strongly correlated [9, 10], and do not consider the quasi-static regime $\mathcal{I} \lesssim 10^{-4}$ where flow appears intermittent and highly heterogeneous [5, 11–13]. In this intermediate range one finds

$$\mu(\mathcal{I}) = \mu_c + a_\mu \mathcal{I}^{\alpha_\mu} \quad (1)$$

$$\phi(\mathcal{I}) = \phi_c - a_\phi \mathcal{I}^{\alpha_\phi}, \quad (2)$$

where μ_c and ϕ_c are non-universal and depend on details of the grains. Experiments on glass beads and sand find exponents $\alpha_\mu \approx \alpha_\phi \approx 1$, consistent with numerical simulations using frictional particles reporting $\alpha_\mu = 0.81$ and $\alpha_\phi = 0.87$ [14]. Despite their importance, constitutive laws (1,2) remain empirical. Building a microscopic framework to explain them would shed light on a range of debated issues, including transient phenomena [2, 15], non-local effects [16, 17], and the presence of S-shaped

flow curves when particles are soft [18–20].

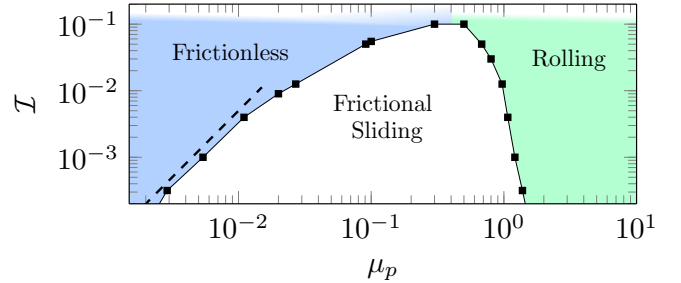


FIG. 1. (Color online) Phase diagram of homogeneous inertial frictional flow at constant pressure. In the frictionless and rolling regimes, most energy is dissipated by inelastic collisions, while in the frictional sliding regime energy dissipation is dominated by sliding. Along the phase boundary, grains dissipate equal amounts of energy in collisions and in sliding. Note that for $\mathcal{I} \gtrsim 0.1$, one enters the dilute regime [8]. The dashed line has slope 2.

To make progress, it is natural to consider the limiting case where particles are *frictionless*, a situation that has received considerable attention in the jamming literature [21–24]. For hard particles, two geometrical results key for inertial flows are as follows. First, as the density increases, the network of contacts becomes more coordinated, implying that motion becomes more constrained. This leads to a divergence of the velocity fluctuations $\langle \delta V \rangle$ when constraints are sufficient to jam the material [25–28]. Thus the contact network acts as a lever, whose amplitude is characterized by the dimensionless number $\mathcal{L} \equiv \langle \delta V \rangle / (\dot{\epsilon}D)$. At the same time, the rate at which new contacts are made increases, and the creation

of each contact affects motion on a growing length scale. These effects imply that velocity fluctuations decorrelate on a strain scale ϵ_v that vanishes at jamming [29]. The theory of Ref. [29], which uses that dissipation can only occur in collisions for frictionless particles, predicts $\alpha_\mu = \alpha_\phi = 0.35$, $\mathcal{L} \sim 1/\sqrt{\mathcal{I}}$ and $\epsilon_v \sim \mathcal{I}$. Encouragingly, these results agree with the numerics of Ref. [30], which found $\alpha_\mu \approx \alpha_\phi \approx 0.38$ and $\mathcal{L} \sim 1/\sqrt{\mathcal{I}}$. However, α_μ and α_ϕ differ significantly from their values for real materials (with frictional grains) stated above, suggesting the presence of different universality classes. Currently, why friction qualitatively affects flows and potentially leads to several universality classes, how many universality classes exist, and what differs between them microscopically are unresolved questions.

In this work we use numerical simulations to answer these questions. We systematically study dense flows over a large range of \mathcal{I} and particle friction coefficient μ_p . By focusing on the microscopic cause of dissipation, we show the existence of three universality classes, as illustrated in Figure 1. At low friction, there exists a frictionless regime in quantitative agreement with the theory of Ref. [29], in particular we establish that $\epsilon_v \sim \mathcal{I}$. As the friction increases, one enters the *frictional sliding* regime, where dissipation is dominated by sliding at contacts instead of collisions, and for which $\epsilon_v \sim \mathcal{I}$ holds true but $\mathcal{L} \sim \mathcal{I}^{-b}$ with $b \approx 0.22$. We relate the exponent b to an exponent characterizing the density of sliding contacts. Finally, at even larger μ_p one enters a *rolling* regime where dissipation is once again dominated by collisions, and where exponents are consistent with those of frictionless particles, both for kinetic observables and constitutive laws. We derive the phase boundary between the frictionless and the frictional sliding regime. Overall, our work explains why friction qualitatively changes physical properties, and paves the way for a future comprehensive microscopic theory of dense granular flows.

Numerical Protocol

To model inertial granular flow of frictional particles, we use a standard discrete element method [31] described in more detail in Methods. We focus on two dimensions (empirically exponents do not appear to depend on dimension, see [29] for a review of the literature on this point). Collisions are computed by modeling grains as viscoelastic disks: when grains overlap at a contact α , they experience elastic and viscous forces \vec{f}_α^e , and \vec{f}_α^v , respectively, leading to a restitution coefficient which we choose to be $e = 0.1$ [32]. These forces can be decomposed into their contributions normal to the contact, $f_\alpha^{N,e}$ and $f_\alpha^{N,v}$, and tangential to the contact, $\vec{f}_\alpha^{T,e}$ and $\vec{f}_\alpha^{T,v}$. The tangential force is imposed to stay inside the Coulomb cone, $|\vec{f}_\alpha^{T,e}| \leq \mu_p f_\alpha^{N,e}$. Contacts that saturate the Coulomb constraint are said to be *sliding*.

The grains are polydisperse with equal numbers of diameter (0.82, 0.94, 1.06, 1.18) [33]. The domain is square and periodic in the x -direction, with rough walls bounding the upper and lower edges. We perform our numerics at imposed global shear rate and constant pressure, following a system preparation described in Appendix 1. We chose the grain stiffness such that the grain relative deformation is set to $\Delta = 10^{-3.8}$, which is small enough to ensure the rigid limit [5], and checked that our results are independent of this parameter. We studied three system sizes $N \in \{1000, 1800, 3700\}$. Results are reported for the largest N ; the absence of finite-size effects is established in Appendix 4.

Partitioning dissipated power

Frictional particles can dissipate energy either through inelastic collisions, or by sliding at frictional contacts. In our contact model, inelasticity is due to the viscous component of contact forces; therefore the collisional dissipation rate is

$$\mathcal{D}_{coll} \equiv \sum_{\alpha \in C} f_\alpha^{N,v} U_\alpha^N + \sum_{\alpha \in C_{NS}} \vec{f}_\alpha^{T,v} \cdot \vec{U}_\alpha^T, \quad (3)$$

where \vec{U}_α is the relative velocity at contact α , decomposed into normal and tangential components, U_α^N and \vec{U}_α^T . Here C denotes all contacts, of number N_C , and C_{NS} denotes non-sliding contacts. The dissipation rate due to sliding is

$$\mathcal{D}_{slid} \equiv \sum_{\alpha \in C_S} \vec{f}_\alpha^{T,e} \cdot \vec{U}_\alpha^T, \quad (4)$$

where C_S is the set of sliding contacts.

In steady state, dissipation must balance the work done at the boundaries. The energy input from the shear stress is $\Omega \sigma \dot{\epsilon}$, where Ω is the system volume. For large systems, additional contributions from fluctuations of the normal position of the wall are insignificant, thus:

$$\Omega \sigma \dot{\epsilon} = \mathcal{D}_{coll} + \mathcal{D}_{slid}. \quad (5)$$

To investigate which source of dissipation dominates in Eq.5, we consider the ratio $\mathcal{D}_{slid}/\mathcal{D}_{coll}$, shown in Fig.2a. As expected, collisional dissipation dominates in the frictionless limit. However, sliding dissipation becomes more important as μ_p is increased from zero, and becomes *dominant* at intermediate friction coefficients and small inertial number. Strikingly, the dependence on μ_p is non-monotonic: when μ_p reaches ≈ 0.2 , this trend abruptly reverses, and $\mathcal{D}_{slid}/\mathcal{D}_{coll}$ *decreases* with μ_p , implying that collisional dissipation dominates as $\mu_p \rightarrow \infty$.

To define phase boundaries, we use the inertial number at which $\mathcal{D}_{slid}/\mathcal{D}_{coll} = 1$, resulting in the phase diagram of Fig.1. From the non-monotonicity of $\mathcal{D}_{slid}/\mathcal{D}_{coll}$ with

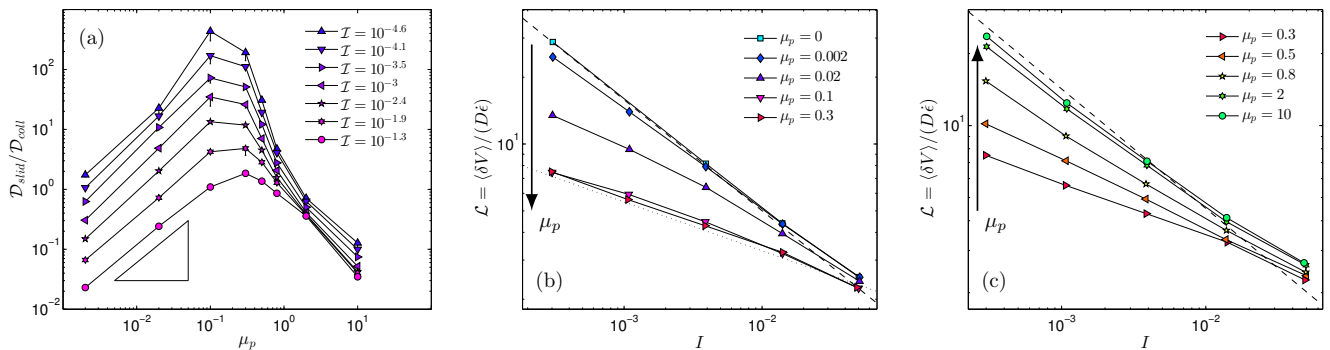


FIG. 2. (Color online) (a) Ratio of dissipation due to sliding, \mathcal{D}_{slid} , to sliding from collisions, \mathcal{D}_{coll} , vs μ_p . The triangle has slope 1. (b,c) Lever \mathcal{L} vs \mathcal{I} , (b) for $\mu_p \leq 0.3$, and (c) for $\mu_p \geq 0.3$. The dashed lines are $\propto \mathcal{I}^{-1/2}$, while the dotted line is $\propto \mathcal{I}^{-0.22}$.

μ_p , this leads to two phase boundaries merging at $\mathcal{I} \approx 0.1$, where the dense flow regime ends [8]. This defines *three* flow regimes: *frictionless*, *frictional sliding*, and *rolling*, where sliding dissipation dominates only in the intermediary regime. Later in this work, we will show that this phase diagram correctly classifies kinetics as well as constitutive laws.

Connecting dissipated power to key kinetic observables

In the rigid limit considered here, collisions become very short in duration, and the power dissipated in collisions can be expressed in terms of microscopic observables [29], as we now recall. We consider rigid grains with a restitution coefficient smaller than one. Each time a particle changes its direction with respect to its neighbors, a finite fraction of its kinetic energy $\sim m\delta V^2$ must be dissipated, where m is the particle mass. Since ϵ_v is the characteristic strain at which velocities decorrelate, this occurs at a rate $\propto \dot{\epsilon}/\epsilon_v$, thus $\mathcal{D}_{coll} \sim N(\dot{\epsilon}/\epsilon_v)m\langle \delta V^2 \rangle$. It is convenient to define a dimensionless dissipation per particle $\tilde{\mathcal{D}}_{coll} \equiv \mathcal{D}_{coll}/(ND^d p \dot{\epsilon})$ (Note that $ND^d p \dot{\epsilon}$ is of order of the injected power $\Omega \sigma \dot{\epsilon}$ because $\sigma \sim p$ in dense flows), thus:

$$\tilde{\mathcal{D}}_{coll} \propto \frac{N(\dot{\epsilon}/\epsilon_v)m\delta V^2}{ND^d p \dot{\epsilon}} \propto \frac{\mathcal{I}^2 \mathcal{L}^2}{\epsilon_v} \quad (6)$$

The sliding dissipation can be directly estimated from its microscopic expression Eq.(4). We assume that the force at the sliding contact is typical, *i.e.* $|f_\alpha^T| = \mu_p f_\alpha^N \sim \mu_p p D^{d-1}$, and that the sliding velocity is of the order of the velocity fluctuation, *i.e.* $|\vec{U}_\alpha^T| \sim \delta V$. These assumptions hold true in the sliding frictional regime where they matter (they eventually break down in the rolling regime where sliding contacts become rare and atypical, see Appendix 3). Defining $\tilde{\mathcal{D}}_{slid} \equiv \mathcal{D}_{slid}/(ND^d p \dot{\epsilon})$, we get the

estimate

$$\tilde{\mathcal{D}}_{slid} \propto \frac{N_c \chi \langle |f^T| \rangle_S \langle |\vec{U}^T| \rangle_S}{ND^d p \dot{\epsilon}} \sim \mu_p \chi \mathcal{L}, \quad (7)$$

where $\langle \cdot \rangle_S$ denotes an average over sliding contacts, whose fraction is χ .

Using Eqs.(5,6,7) we now get the following constraints on the different regimes:

$$1 \sim \frac{\mathcal{I}^2 \mathcal{L}^2}{\epsilon_v} \quad \text{Frictionless, Rolling} \quad (8)$$

$$1 \sim \mu_p \chi \mathcal{L}, \quad \text{Frictional Sliding} \quad (9)$$

We now test these scaling relations and use them to compute the boundary of the frictionless regime.

Measuring kinetic observables

We measure the lever effect defined as $\mathcal{L} \equiv \langle \delta V \rangle / (\dot{\epsilon} D)$, where $\langle \delta V \rangle$ is the typical magnitude of velocity fluctuation about the mean velocity profile [34]. Our results are shown in Fig.2bc. For any μ_p , \mathcal{L} grows as $\mathcal{I} \rightarrow 0$. In the frictionless limit, we find $\mathcal{L} \propto \mathcal{I}^{-0.50}$, in agreement with earlier results [30] and the prediction [29]. A striking result is that the amplitude of this growth is non-monotonic in μ_p , with a minimum around $\mu_p \approx 0.2$, thus closely paralleling the phase diagram of Fig.1. Moreover, in the $\mu_p \rightarrow \infty$ limit, the divergence is again close to $\mathcal{L} \propto \mathcal{I}^{-0.50}$. In contrast, curves that are fully in the frictional sliding regime, as occurs for $\mu_f = 0.1$ or $\mu_f = 0.3$, are well fitted by $\mathcal{L} \propto \mathcal{I}^{-0.22}$.

We now turn to the strain scale ϵ_v beyond which a particle loses memory of its velocity. It can be extracted from the decay of the autocorrelation function [35]

$$C(\epsilon) = \langle V_i^y(0) V_i^y(\epsilon) \rangle, \quad (10)$$

where we use the vertical component of velocity at particle i , V_i^y , averaged over all particles and initial time steps.

The normalized correlation function $\tilde{C}(\epsilon) = C(\epsilon)/C(0)$ is shown for $\mu_p = 0.02$ and various \mathcal{I} in Fig.3a. We see that beyond a scale ϵ_v , $\tilde{C}(\epsilon)$ decays as a power-law, as observed numerically in over-damped suspensions [29, 35]. For all μ_p , $\tilde{C}(\epsilon)$ has a similar form; we find that for $\epsilon \lesssim 10^{-2}$ it is well-fitted by $[1 + (\epsilon/\epsilon_v(\mathcal{I}))^\nu]^{-\eta}$, with $\nu = 1.1$ and η dependent on μ_p . By rescaling ϵ to obtain a collapse, shown in Fig.3b, we obtain the scale ϵ_v . Repeating this process for all μ_p leads to the results shown in Fig.4a,b; details are shown in Appendix 2. We observe that for all \mathcal{I} and all μ_p , we have approximately $\epsilon_v \approx \mathcal{I}$, although our best exponent for the rolling regime is closer to $\epsilon_v \approx \mathcal{I}^{1.25}$. This result is thus in excellent agreement with the prediction of [29] for the frictionless case, and appears to be more general.

Finally, the fraction of sliding contacts χ is shown in Fig.4c. For each μ_p , χ decays as $\mathcal{I} \rightarrow 0$. We see that in the frictionless regime, $\chi \approx 1$, as expected. In the frictional sliding and rolling regimes, χ decays as a power-law as \mathcal{I} is decreased. For the frictional regime, such as $\mu_p = 0.3$, data are well-fitted by $\chi \sim \mathcal{I}^{0.20}$. In the rolling regime instead the decay appears faster, with $\chi \sim \mathcal{I}^{0.44}$ for $\mu_p = 10$.

Our results are summarized in Table I, which shows the exponents characterizing the different regimes. Tests for the scaling relations Eqs.(8,9) are also summarized; data and predictions are found to be consistent.

Regime boundaries

We can now estimate the parameters for which the frictionless regime breaks down. Since in that regime $\mathcal{L} \sim \mathcal{I}^{-0.5}$, $\epsilon_v \sim \mathcal{I}$, and $\chi \sim 1$, we have according to Eqs.(6,7) $\mathcal{D}_{slid}/\mathcal{D}_{coll} \sim \mu_p \mathcal{I}^{-0.5}$. The dependence of this ratio on μ_p is directly supported by Fig.2a. The frictionless regime must break down at an inertial number \mathcal{I}_c where this ratio is of order one, yielding $\mathcal{I}_c \sim \mu_p^2$ in agreement with Fig.1.

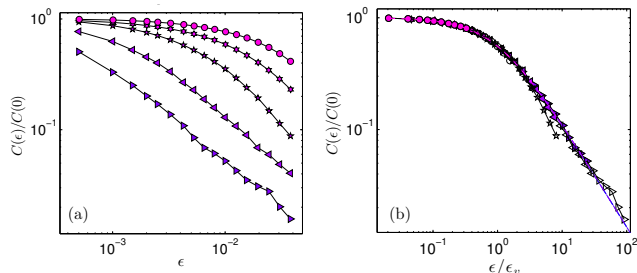


FIG. 3. (Color online) Autocorrelation of particle velocities, $\tilde{C}(\epsilon) = \langle V_i^y(0)V_i^y(\epsilon) \rangle / \langle V_i^y(0)^2 \rangle$ for $\mu_p = 0.02$ and \mathcal{I} from $10^{-3.5}$ (up triangles) to $10^{-1.3}$ (circles) (symbols as in Fig 2a). (a) $\tilde{C}(\epsilon)$ vs ϵ . (b) $\tilde{C}(\epsilon)$ vs ϵ/ϵ_v . In (b), unfilled symbols correspond to strains larger than 0.01, not used for fitting, and the solid line shows the fitted form.

Regime	Relation	Prediction	Measured
Frictionless	$\mathcal{L} \sim \mathcal{I}^{-b}$	$b = 1/2$	$b = 0.50$
	$\epsilon_v \sim \mathcal{I}^c$	$c = 1$	$c = 1.05$
Frictional Sliding	$\mathcal{L} \sim \mathcal{I}^{-b}$		$b = 0.22$
	$\epsilon_v \sim \mathcal{I}^c$		$c = 0.95$
	$\chi \sim \mathcal{I}^d$	$d = b$	$d = 0.20$
Rolling	$\mathcal{L} \sim \mathcal{I}^{-b}$		$b = 0.50$
	$\epsilon_v \sim \mathcal{I}^c$	$c = 2 - 2b$	$c = 1.25$
	$\chi \sim \mathcal{I}^d$		$d = 0.42$

TABLE I. Summary of scaling behavior in three regimes. Predictions for the frictionless regime are quoted from the theory of [29], while the other predictions are Eqs.(8,9). In the frictional sliding regime, scalings are taken for the extremal value $\mu_p = 0.3$, while for the rolling regime, scalings are taken from $\mu_p = 10$.

Inside the sliding regime, we have $\epsilon_v \approx \mathcal{I}$. To determine the transition to a rolling regime, we note from Eq.(9) that $\mathcal{D}_{slid}/\mathcal{D}_{coll} \sim 1/(\mathcal{I}\mathcal{L}^2) \sim \mu_p^2\chi^2/\mathcal{I}$. We observe that the product $\chi\mu_p$ decays with large μ_p at fixed \mathcal{I} (data not shown). Thus, although the dissipation of each sliding contact grows with the friction coefficient, fewer and fewer contacts slide as μ_f becomes very large, and the latter effect dominates when the friction coefficient is large enough. This qualitatively explains the observed non-monotonic behavior with friction coefficient.

Constitutive relations

Experimentally, the most accessible quantities are the constitutive relations $\mu(\mathcal{I})$ and $\phi(\mathcal{I})$, which we show in Fig.5. As shown in the inset to Fig.5a, the critical values $\mu_c = \mu(0)$ and $\phi_c = \phi(0)$ [36] display a smooth behavior with μ_p , and saturate both in the frictionless regime at small μ_p , and the rolling regime at large μ_p . This is consistent with previous results on isotropic packings [37] and other works [38].

To discuss universality classes, it would seem appropriate to measure the exponents α_μ and α_ϕ entering Eqs.(1,2). However, these exponents are much harder to measure than those summarized in Table I, because of the presence of fitting parameters μ_c and ϕ_c , and very large systems are required for a reliable measurement [30]. Instead we simply consider the cases $\mu_p = 0$, $\mu_p = 0.3$, and $\mu_p = 10$ for which our data are respectively in the frictionless, frictional sliding, and rolling regimes. In the main panel of Fig.5 it appears that the curves for $\mu_p = 10$ and $\mu_p = 0$ are parallel to each other, suggesting that they display the same exponents α_μ and α_ϕ , while the curve for $\mu_p = 0.3$ has a different shape, in agreement with the empirical results reported in the introduction. We test this view in the inset to Fig.5b, by subtracting off the critical stress anisotropy μ_c . We indeed confirm that

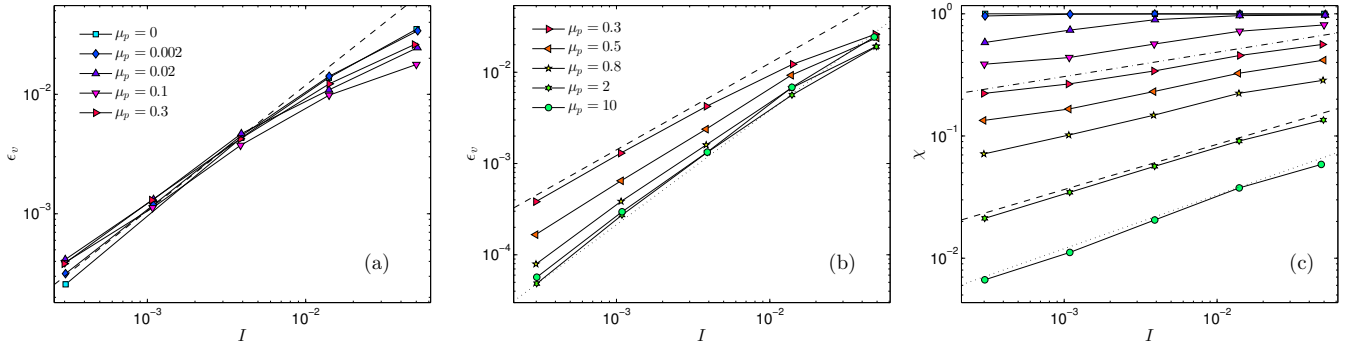


FIG. 4. (Color online) Decorrelation strain scale, ϵ_v , (a) vs \mathcal{I} for $\mu_p \leq 0.3$, and (b) vs \mathcal{I} for $\mu_p \geq 0.3$. The dashed line is $\propto \mathcal{I}^{1.05}$ in (a) and $\propto \mathcal{I}^{0.95}$ in (b). The dotted line in (b) is $\propto \mathcal{I}^{1.25}$. (c) The fraction of sliding contacts, χ , vs \mathcal{I} . Dotted, dashed, and dot-dashed lines have slopes 0.44, 0.37, and 0.20, respectively.

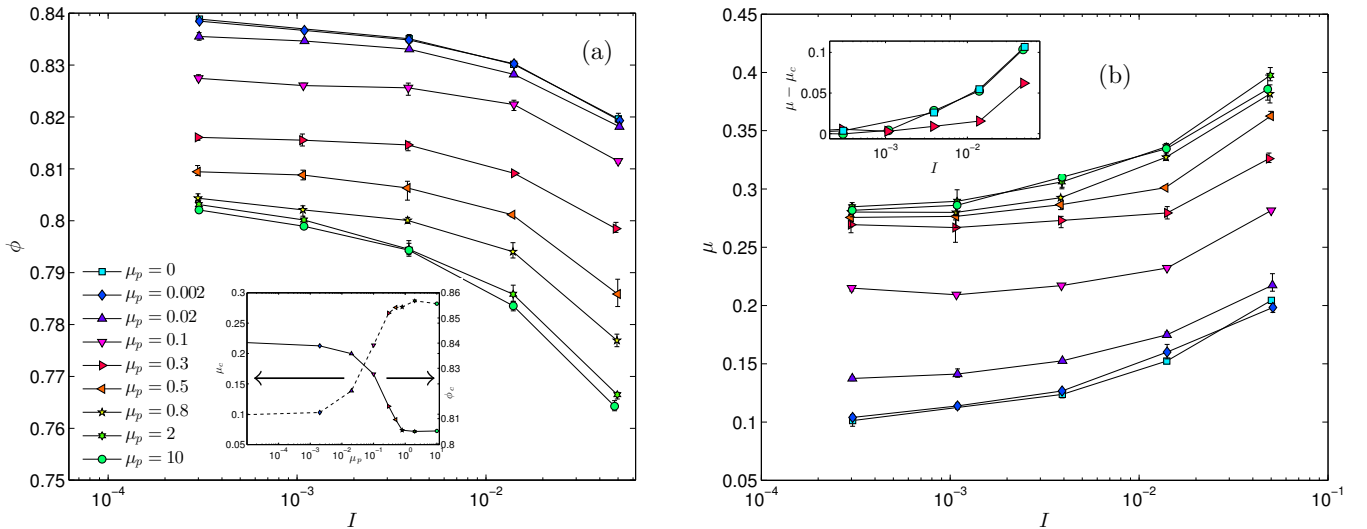


FIG. 5. (Color online) (a) Volume fraction ϕ vs \mathcal{I} . Inset shows $\mu_c = \mu(0)$ vs μ_p (left axis, dashed), and $\phi_c = \phi(0)$ vs μ_p (right axis, solid). Note that the frictionless results are plotted at $\mu_p = 10^{-5}$. (b) Effective friction μ vs \mathcal{I} . Inset shows non-monotonic behavior of $\mu(\mathcal{I}) - \mu_c$, for $\mu_p = 0, 0.3, 10$.

$\delta\mu(\mathcal{I}) \equiv \mu(\mathcal{I}) - \mu_c$ is nearly identical in the frictionless and rolling regimes (the points overlap), and definitely distinct from its behavior in the frictional sliding regime. This observation supports further our claim for three distinct universality classes where scaling behavior differs, both for microscopic and macroscopic observables.

Discussion

Our work supports the classification of dense inertial granular flows in three regimes, in a phase diagram spanned by the friction coefficient μ_f and the distance to jamming, characterized by the inertial number \mathcal{I} . From considerations of the microscopic cause of dissipation, we have shown that its nature must change as the friction coefficient μ_f increases from zero. One eventually leaves

the frictionless regime to enter in the frictional sliding regime, where both the kinetics and constitutive relations differ. As μ_f increases further, fewer and fewer contacts slip, and one enters the rolling regime where collisions once again dominate dissipation, and where exponents are consistent with that of the frictionless regime.

Experimentally, these results could be tested by measuring the correlation function $C(\epsilon) = \langle V_i^y(0)V_i^y(\epsilon) \rangle$, which captures both the lever amplitude \mathcal{L} (at $\epsilon = 0$) and the characteristic strain ϵ_v . This will require a sufficient resolution in the strain ϵ that can be probed. It will be very interesting to vary the friction coefficient of the particles in these studies. If typical beach sand has $\mu_p \approx 0.3$, materials exist both with a larger μ_p , and with μ_p an order of magnitude smaller.

On the theoretical level, a theory of the frictional sliding regime, the most important in practice, is still lack-

ing. Theory should explain the singularities in the constitutive laws $\phi(\mathcal{I})$ and $\mu(\mathcal{I})$, the scaling of kinetic observables $\epsilon_v(\mathcal{I})$ and $\mathcal{L}(\mathcal{I})$, and the transition to a rolling regime. Why the latter appears to behave as the frictionless regime as far as exponents are concerned also needs to be clarified further, beyond their similarity in dissipation mechanism established here.

Finally, this work could be extended in several directions. It would be very interesting to measure the kinetic quantities presented here in the quasi-static regime of very slow flows $\mathcal{I} \lesssim 10^{-4}$ where intermittency appears [5, 11–13]. Similar extensions could be done with respect to particle shape, where local ordering is important [39, 40], and particle softness, where the shape of the flow curve can become sigmoidal, leading to hysteresis [18–20]. Last, over-damped suspensions present the same problem as inertial flows: various numerical studies have focused on frictionless particles [14, 25, 41–44], which appear consistent with the theory developed in [29]. In that case, it is currently unclear if friction qualitatively affects physical properties, as experiments [45, 46] and numerics [47] where friction is present are reasonably compatible with these studies. Building a phase diagram analogous to Fig.1, comparing the amplitude of sliding dissipation to other sources, would resolve this issue.

ACKNOWLEDGMENTS

We acknowledge discussions with M. Cates, G. Düring, Y. Forterre, E. Lerner, J. Lin, B. Metzger, M. Müller, O. Pouliquen, A. Rosso, and L. Yan. This work was supported primarily by the Materials Research Science and Engineering Center (MRSEC) Program of the National Science Foundation under Award No. DMR-0820341.

METHODS

Simulations are performed with a standard Discrete Element Method code [31], which integrates Newton's equations of motion for each grain. The square domain of size $L_x \times L_y$ is periodic in the x -direction and has upper and lower walls. The walls are created from the same polydisperse mixture as the bulk, staggered to create roughness. The walls obey an equation of motion

$$M \frac{d^2 \vec{r}}{dt^2} + \eta \frac{d\vec{r}}{dt} = \vec{F}_{bulk} + \vec{F}_{ext}, \quad (11)$$

where M is mass, η is a damping coefficient, \vec{F}_{bulk} is the force from the bulk of the packing, and \vec{F}_{ext} is an external applied force. The bulk-wall interactions are via contact forces, exactly as in the bulk. The external force in the y -direction is constant, such that $F_{ext}^{\pm y} = \mp PL_x$ on the top (+) and bottom (-) walls. In the x -direction, the external force is chosen to impose a constant velocity $\pm V_w$, and

hence a constant global shear rate $\dot{\epsilon} = 2V_w/L_y$, up to fluctuations in L_y .

We seek to make the flow as homogeneous as possible. Following [5], we set $\eta = \sqrt{mk}$, where k is the spring constant for particle-particle elastic interactions, and m the mean particle mass. We tested the dependence of the results on M . When $M/m \sim 1$, the wall equation Eq.(11) is dominated by the viscous term, and can exhibit long transients. We therefore set $M/m = 50$, so that the wall density and particle density are the same order; this minimized transients.

With this choice of wall parameters, we find that steady states are achieved where the relative pressure fluctuations range from 1% at $\mathcal{I} \sim 10^{-5}$ to 20% at $\mathcal{I} \sim 0.1$; thus the mean particle overlap $\Delta \propto P/k$ is fixed to within this precision.

To prepare homogeneous steady states, initially isotropic packings are created from a gas at volume fraction $\phi_0 = 0.5$, and then sheared for a pre-strain ϵ_0 . As discussed in Appendix 1, an analysis of Eq.11, leads to our choosing $\epsilon_0 = \max(0.2, \Delta^{-1/2}\mathcal{I})$, which we checked ensures that a steady state is reached. After this initial strain, without collecting data, we strain the systems for $\epsilon = 0.3$, collecting data every $\delta\epsilon = 5 \times 10^{-4}$.

In all cases, we discard runs that are not sufficiently homogeneous. As a first criterion, we exclude simulation runs where the mean velocity profile has a shear band. As a second criterion, we find for certain parameter values that resonant elastic waves bounce back and forth between the walls at very high frequency, as discussed in [48]. Resolution of these waves requires a much smaller time step than is needed otherwise, so we do not include these runs. Details of these criteria appear in Appendix 1.

-
- [1] P. G. de Gennes, Reviews of Modern Physics **71**, S374 (1999).
 - [2] B. Andreotti, Y. Forterre, and O. Pouliquen, *Granular media: between fluid and solid* (Cambridge University Press, 2013).
 - [3] R. Nedderman, *Statics and Kinematics of Granular Materials* (Cambridge, Cambridge, U.K., 1992).
 - [4] G. MiDi, The European Physical Journal E: Soft Matter and Biological Physics **14**, 341 (2004-08-01).
 - [5] F. da Cruz, S. Emam, M. Prochnow, J.-N. Roux, and F. m. c. Chevoir, Phys. Rev. E **72**, 021309 (2005).
 - [6] G. Lois, A. Lemaitre, and J. M. Carlson, Physical Review E **72**, 051303 (2005).
 - [7] Y. Forterre and O. Pouliquen, Annual Review of Fluid Mechanics **40**, 1 (2008).
 - [8] E. Azéma and F. Radjai, Physical review letters **112**, 078001 (2014).
 - [9] F. Radjai and S. Roux, Phys. Rev. Lett. **89**, 064302 (2002).
 - [10] O. Pouliquen, Physical review letters **93**, 248001 (2004).

- [11] N. Kruyt and S. Antony, Physical Review E **75**, 051308 (2007).
- [12] J. Gaume, G. Chambon, and M. Naaim, Physical Review E **84**, 051304 (2011).
- [13] S. Henkes, D. A. Quint, Y. Fily, and J. Schwarz, arXiv preprint arXiv:1508.00122 (2015).
- [14] P.-E. Peyneau, *Etude du comportement et du compactage de pates granulaires par simulation numerique discrete*, Ph.D. thesis, Ecole des Ponts ParisTech (2009).
- [15] D. Bi, J. Zhang, B. Chakraborty, and R. Behringer, Nature **480**, 355 (2011).
- [16] M. Bouzid, M. Trulsson, P. Claudin, E. Clément, and B. Andreotti, Phys. Rev. Lett. **111**, 238301 (2013).
- [17] D. L. Henann and K. Kamrin, Proceedings of the National Academy of Sciences **110**, 6730 (2013).
- [18] M. Otsuki and H. Hayakawa, Physical Review E **83**, 051301 (2011).
- [19] M. P. Ciamarra, R. Pastore, M. Nicodemi, and A. Coniglio, Physical Review E **84**, 041308 (2011).
- [20] M. Grob, C. Heussinger, and A. Zippelius, Physical Review E **89**, 050201 (2014).
- [21] C. S. O'Hern, L. E. Silbert, A. J. Liu, and S. R. Nagel, Phys. Rev. E **68**, 011306 (2003).
- [22] M. Wyart, Annales de Phys **30**, 1 (2005).
- [23] A. J. Liu, S. R. Nagel, W. van Saarloos, and M. Wyart, "The jamming scenario: an introduction and outlook," in *Dynamical heterogeneities in glasses, colloids, and granular media*, edited by L. Berthier, G. Biroli, J. Bouchaud, L. Cipeletti, and W. van Saarloos (Oxford University Press, Oxford, 2010).
- [24] M. van Hecke, Journal of Physics: Condensed Matter **22**, 033101 (2010).
- [25] E. Lerner, G. Düring, and M. Wyart, Proceedings of the National Academy of Sciences **109**, 4798 (2012).
- [26] G. Düring, E. Lerner, and M. Wyart, Soft Matter **9**, 146 (2013).
- [27] G. Düring, E. Lerner, and M. Wyart, Physical Review E **89**, 022305 (2014).
- [28] B. Andreotti, J.-L. Barrat, and C. Heussinger, Phys. Rev. Lett. **109**, 105901 (2012).
- [29] E. DeGiuli, G. Düring, E. Lerner, and M. Wyart, Physical Review E **91**, 062206 (2015).
- [30] P.-E. Peyneau and J.-N. Roux, Physical review E **78**, 011307 (2008).
- [31] P. A. Cundall and O. D. Strack, Geotechnique **29**, 47 (1979).
- [32] The choice of restitution coefficient has little effect on flow in the dense regime, see [5, 38].
- [33] The same mixture used in [20].
- [34] In simulations with walls, the mean velocity profile is not linear [5], therefore this differs slightly from the non-affine velocity [29].
- [35] P. Olsson, Phys. Rev. E **81**, 040301 (2010).
- [36] μ_c and ϕ_c were determined with additional runs down to $\mathcal{I} = 10^{-4.6}$.
- [37] K. Shundyak, M. van Hecke, and W. van Saarloos, Phys. Rev. E **75**, 010301 (2007).
- [38] S. Chialvo, J. Sun, and S. Sundaresan, Physical Review E **85**, 021305 (2012).
- [39] E. Azéma and F. Radjaï, Physical Review E **81**, 051304 (2010).
- [40] E. Azéma, N. Estrada, and F. Radjai, Physical Review E **86**, 041301 (2012).
- [41] P. Olsson and S. Teitel, Phys. Rev. Lett. **99**, 178001 (2007).
- [42] P. Olsson and S. Teitel, Physical Review E **83**, 030302 (2011).
- [43] C. Heussinger and J.-L. Barrat, Phys. Rev. Lett. **102**, 218303 (2009).
- [44] P. Olsson, arXiv preprint arXiv:1503.08480 (2015).
- [45] F. Boyer, E. Guazzelli, and O. Pouliquen, Phys. Rev. Lett. **107**, 188301 (2011).
- [46] S. Dagois-Bohy, S. Hormozi, É. Guazzelli, and O. Pouliquen, Journal of Fluid Mechanics **776**, R2 (2015).
- [47] M. Trulsson, B. Andreotti, and P. Claudin, Physical review letters **109**, 118305 (2012).
- [48] M. Trulsson, M. Bouzid, P. Claudin, and B. Andreotti, EPL (Europhysics Letters) **103**, 38002 (2013).

APPENDIX

Appendix 1. Numerical Simulations

Here we provide several details of the numerical simulations. To determine an appropriate pre-strain scale ϵ_0 , consider the y -direction bulk-wall force on the top wall, F_{bulk}^{+y} . This is a spring-like force, since it results from the elastic interactions between the particles adjacent to the wall, and the wall itself, but with a nontrivial spring constant. It can be estimated from the law $\phi_c - \phi \propto \mathcal{I}^{\alpha_\phi}$. Indeed, linearizing this law around a mean volume fraction $\bar{\phi}$ and mean pressure \bar{P} , we find $P - \bar{P} \propto -\dot{\epsilon}^2(\phi_c - \bar{\phi})^{-1/\alpha_\phi - 1}(y_w - L_y/2)/L_y$, where L_y is the mean thickness of the domain and we used $(\phi - \bar{\phi})/\bar{\phi} = -(y_w - L_y/2)/(L_y/2)$. Hence the bulk-wall force is approximately $F_{bulk}^{+y} \sim PL_x \sim -k_w(y_w - L_y/2)$ with $k_w \sim \dot{\epsilon}^2(\phi_c - \bar{\phi})^{-1/\alpha_\phi - 1} \sim \bar{P}(\phi_c - \bar{\phi})^{-1}$. The strain scale associated with the damping term in Eq.(11) is then $\epsilon_0 \sim \dot{\epsilon}\eta/k_w \sim \Delta^{-1/2}\mathcal{I}(\phi_c - \bar{\phi})$, where $\Delta = p/k$. We conservatively take $\epsilon_0 = \max(0.2, \Delta^{-1/2}\mathcal{I})$.

Our two criteria for ensuring homogeneity of the flows are that there is no static shear band, and that the walls are not in resonant motion. To test for a shear band, we compute the deviation of the mean velocity profile from a linear one, $\delta v(y) = v(y) - \dot{\epsilon}y$, and compute its normalized standard deviation, $\langle (\delta v(y) - \langle \delta v \rangle)^2 \rangle_y / (L_y \dot{\epsilon})^2$. For a perfect shear band, this is $1/\sqrt{12} = 0.29$; we discard runs where it exceeds 0.2.

For certain parameter values, resonant elastic waves bounce back and forth between the walls at very high frequency, as discussed in [48]. Resolution of these waves requires a much smaller time step than is needed otherwise, and in our code they display an unphysical alternation of the velocity of the wall from positive to negative values at each strain increment where we save data. Therefore we compute a normalized numerical derivative of the vertical wall velocity, $O = (V_w(\epsilon + \Delta\epsilon) - V_w(\epsilon))/(\Delta\epsilon\langle\delta V\rangle)$, where V_w is the wall velocity (for brevity, here we include only one wall), and $\langle\delta V\rangle$ is the velocity scale of grains in the bulk, computed from their fluctuations. We find that for well-behaved runs, $O\mathcal{I} \sim 1$, while for numerically unstable ones, $O\mathcal{I} > 10000$. Therefore we exclude runs with $O\mathcal{I} > 2000$. We checked that the few runs so excluded

agree in their location in phase space with the theory of [48].

Appendix 2. Velocity autocorrelation function

In the main text we introduced the autocorrelation function

$$C(\epsilon) = \langle V_i^y(0)V_i^y(\epsilon) \rangle, \quad (12)$$

in terms of the vertical component of velocity at particle i , V_i^y , averaged over all particles and all initial time steps for a given strain increment ϵ . In Fig.6, we show $C(\epsilon)/C(0)$ for several values of μ_p . The values of η are listed in Table II.

μ_p	0	0.002	0.02	0.1	0.3	0.5	0.8	2	10
η	1.2	1.2	0.85	0.5	0.6	0.6	0.65	0.75	0.85

TABLE II. Exponent η in fit of $C(\epsilon)/C(0)$.

Appendix 3. Sliding dissipation in rolling regime

In the rolling regime, only a small subset of contacts are sliding, as shown in Fig.4c. This raises the possibility that the forces and velocities at these contacts may be atypical of the system as a whole. We investigate this with the quantities $\zeta \equiv \langle f^N \rangle_S / (pD^{d-1})$, and $\mathcal{L}_T = \langle |\vec{U}^T| \rangle_S / (D\dot{\epsilon})$, where $\langle \cdot \rangle_S$ denotes an average over sliding contacts. As shown in Fig.7, atypical behavior of sliding contacts is indeed shown for large μ_p , and in fact we find in this regime that both ζ and $\mathcal{L}_T/\mathcal{L}$ show power-law behavior. In particular, for $\mu_p = 2$ we find $\zeta \sim \mathcal{I}^{0.31}$ and $\mathcal{L}_T/\mathcal{L} \sim \mathcal{I}^{-0.29}$, while for $\mu_p = 10$ we find $\zeta \sim \mathcal{I}^{0.43}$ and $\mathcal{L}_T/\mathcal{L} \sim \mathcal{I}^{-0.34}$. The quantities ζ and $\mathcal{L}_T/\mathcal{L}$ would be needed for an accurate scaling estimate of sliding dissipation in the rolling regime.

Appendix 4. N dependence

In the main text, we reported results for $N \approx 3700$. Here we discuss how our results depend on N . We show representative plots for $N \approx 1000, 1800, 3700$ at several values of μ_p and several quantities in Fig.8. We see that χ and $\mathcal{D}_{slid}/\mathcal{D}_{coll}$ are independent of N at the two largest values studied, while \mathcal{L} displays a mild, systematic dependence. This behavior is representative for all values of μ_p . In all cases the minor dependence in \mathcal{L} does not affect the scaling behavior of observables, and in particular the phase diagram is not affected.

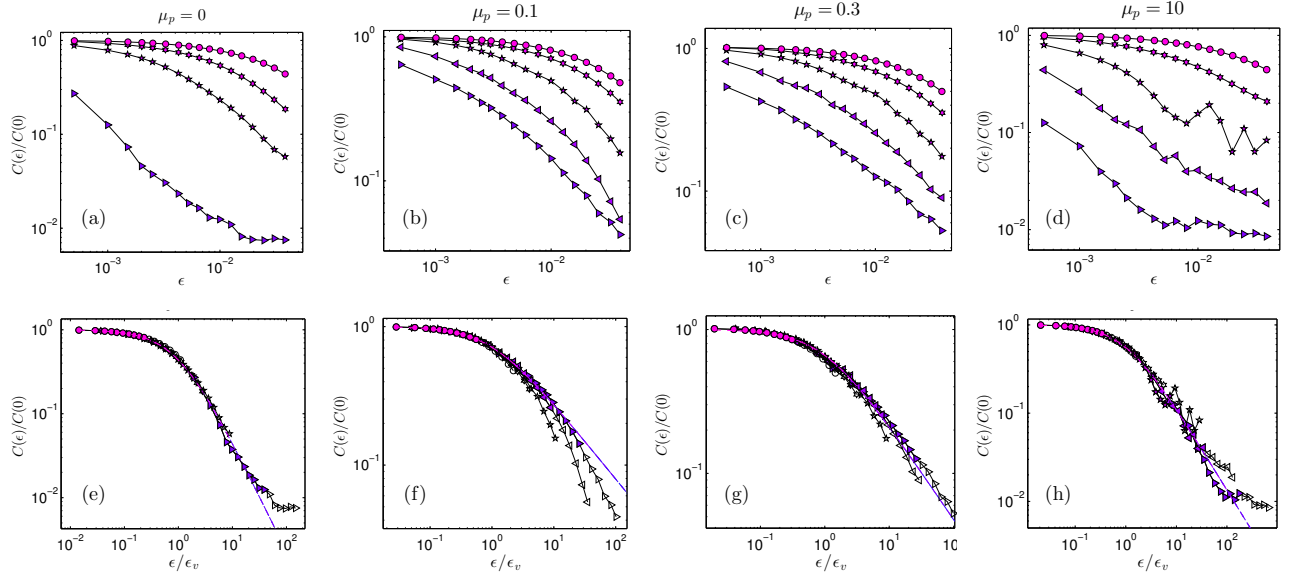


FIG. 6. (Color online) Autocorrelation of particle velocities, $C(\epsilon) = \langle V_i^y(0)V_i^y(\epsilon) \rangle$ for indicated μ_p and \mathcal{I} from $10^{-3.5}$ (up triangles) to $10^{-1.3}$ (circles) (symbols as in Fig 2a). (a-d) $C(\epsilon)/C(0)$ vs ϵ . (e-h) $C(\epsilon)/C(0)$ vs ϵ/ϵ_v . In (e-h), unfilled symbols correspond to strains larger than 0.01, not used for fitting, and the solid line shows the fitted form.

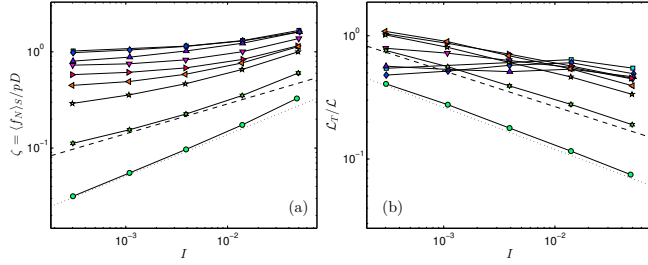


FIG. 7. (Color online) (a) ζ vs \mathcal{I} . Dotted and dashed lines have slopes 0.43 and 0.31, respectively. (b) $\mathcal{L}_T/\mathcal{L}$ vs \mathcal{I} . Dotted and dashed lines have slopes -0.34 and -0.29, respectively.

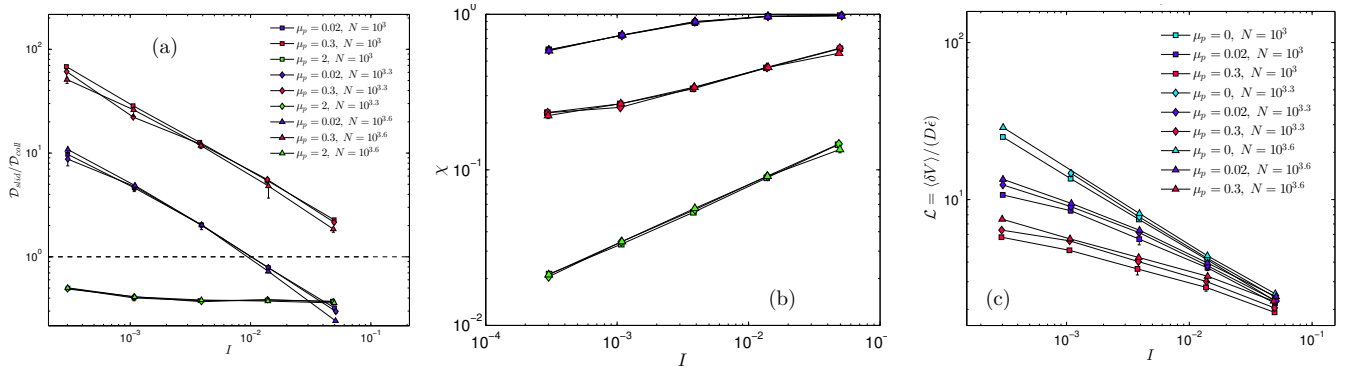


FIG. 8. (Color online) N -dependence of observables. (a) Dissipation ratio vs \mathcal{I} . (b) χ vs \mathcal{I} . (c) \mathcal{L} vs \mathcal{I} .